Research Square

Preprints are preliminary reports that have not undergone peer review.
They should not be considered conclusive, used to inform clinical practice,
or referenced by the media as validated information.

Beyond Qualitative Diagnosis of Li Plating in Li-ion Batteries: A Critical-State Metric from Electrochemical Impedance Spectroscopy

Wenxuan Hu
Xiamen University
Jianrong Lin
Xiamen University
Yingao Zhou
Xiamen University
Hongxin Lin
Xiamen University
Wenhao Wu
Xiamen University
Ying Lin
Xiamen University
Yonggang Hu
Xiamen University
Yufan Peng
Xiamen University
Xiaozhe Yu
Xiamen University
Jinding Liang
Contemporary Amperex Technology Co., Ltd
Yimin Wei
Contemporary Amperex Technology Co., Ltd
Yanting Jin
Xiamen University
Zhengliang Gong
Xiamen University
Yong Yang
yyang@xmu.edu.cn

Xiamen University

Research Article

Keywords: Lithium-ion batteries, Li plating quantification, dynamic electrochemical impedance spectroscopy, operando solid-state NMR, battery aging

Posted Date: April 24th, 2026

DOI: https://doi.org/10.21203/rs.3.rs-9420766/v1

License: This work is licensed under a Creative Commons Attribution 4.0 International License.
Read Full License

Additional Declarations: No competing interests reported.

Beyond Qualitative Diagnosis of Li Plating in Li-ion Batteries: A Critical-State Metric from Electrochemical Impedance Spectroscopy

Wenxuan Hu,[1 #] Jianrong Lin,[2 #] Yingao Zhou,[1] Hongxin Lin,[1] Wenhao Wu,[1] Ying Lin,[1] Yonggang Hu,[1] Yufan Peng,[1,3] Xiaozhe Yu,[1] Jinding Liang,[4] Yimin Wei,[4] Yanting Jin[1,3], Zhengliang Gong,[2] Yong Yang[1,3*]

[1]State Key Laboratory for Physical Chemistry of Solid Surfaces, Department of Chemistry, College of Chemistry and Chemical Engineering, Xiamen University, Xiamen, 361005, China

[2]College of Energy, Xiamen University, Xiamen, 361005, China

[3]Innovation Laboratory for Sciences and Technologies of Energy Materials of Fujian Province (IKKEM), Xiamen 361005, China

[4]21C Innovation Laboratory, Contemporary Amperex Technology Co., Ltd, Ningde 352100, China.

[#] Wenxuan Hu and Jianrong Lin contributed equally to this work

[*] Corresponding author

Yong Yang

Xiamen University

Email: yyang@xmu.edu.cn

Abstract: Lithium-ion batteries (LIBs) deployed in smart grid applications require extended cycle life and predictable safety performance through advanced battery management systems. Li plating, a major cause of capacity fade and thermal runaway, poses a critical challenge owing to its transient, heterogeneous nature and the lack of operando quantitative detection tools. To address this gap, we establish an operando quantitative framework for real-time monitoring of Li plating on graphite anodes. The proposed critical Li-plating areal capacity (q_{Li}), derived from dynamic electrochemical impedance spectroscopy (DEIS) enables precise calculation of Li deposition kinetics under various charging protocols. Multi-modal validation through operando solid-state nuclear magnetic resonance (ssNMR)-DEIS combined measurements, incremental capacity analysis (ICA), and mass spectrometry titration (MST) demonstrates the method's robustness with high accuracy ($R^2 > 0.97$) across diverse charging conditions and battery configurations. Furthermore, accelerated aging under coupled conditions identifies critical thresholds: mild Li plating not only accelerates capacity fade, but also drives Li plating-boundary migration beyond the critical q_{Li}, thereafter causing capacity plunge. This work advances both methodological frameworks—by establishing the first operando quantification platform for Li plating—and battery safety management strategies, offering safety alerting and adaptive charging protocols to keep plating below q_{Li} and thereby extend cycle life.

Keywords: Lithium-ion batteries; Li plating quantification; dynamic electrochemical impedance spectroscopy; operando solid-state NMR; battery aging

1. Introduction

Over the past decade, the global market of Lithium-ion batteries (LIBs) has been growing by leaps and bounds. Vaulting from consumer electronics to electric vehicles, and then to grid-level energy storage system, LIBs are already ubiquitous in human life. However, risks beneath prosperity should not be ignored, as the increasing safety accidents raise doubts on the safety use and management of LIBs. Among all the causes, Li plating is one of the most detrimental factors that commonly exist in LIBs, which may penetrate the separator and lead to internal short-circuit [1-3]. Therefore, this phenomenon draws great attention not only from the academia but also the industry. Given the complex working conditions of LIBs and a current situation pursuing faster charging rates, it has become an important task to monitor in real time whether Li plating occurs, the amounts and reversibility of the deposited Li, and to evaluate its impact on the battery life [4-8]. However, the coupling of Li intercalation and Li plating in electrochemical signals leads to the inherent concealment of Li plating [9-11]. Furthermore, its dynamic evolution over time and complex effects of operating conditions (temperature-rate coupling) on its characteristic features further complicate its detection [12-14]. The development of non-destructive methods for the qualitative and even quantitative monitoring of Li plating under real-world operating conditions remains a substantial and urgent task.

Currently, the majority of studies concentrate on providing a noninvasive and operando approach for detecting the onset of Li plating on graphite anodes [15-17], such as impedance-based methods [18-23], pressure-based methods [24-25], voltage-based methods [26-27], capacity-based methods [28-29], and other physics features-based methods [30-31]. These works capture the alterations in certain electrochemical and physical signals induced by Li plating to indicate its occurrence.

Among them, impedance-based method delivers great sensitivity and accuracy due to the strong decoupling capability of EIS on various physico-electrochemical processes. Several physical parameters, including SEI resistance [18], charge transfer resistance (R_{ct}) [19-20], double layer capacitance (C_{dl}) [21], time constant of charge transfer process [22], have been proposed to indicate the Li plating occurrence. However, the quantitative potential of impedance on Li plating remains controversial, as the quantitative relationship between impedance and capacity of plated Li metal is difficult to explain from a physical essence perspective. Zhang's group developed the dynamic capacitance measurement method to quantify Li plating through the variation of C_{dl} during charging, though it has yet to establish a rigorous quantitative relationship under complex conditions and lacks comprehensive validation [21]. Despite impedance-based methods, the capacity-based method also serves as a potential approach for the quantification of Li plating, yet it still has considerable limitations. Wang' group employed the incremental capacity peak of Li stripping to quantify reversible efficiency of over-lithiated Li in Li/graphite half-cells [29]. However, the capacity-based method is mostly a post-hoc analysis rather than operando method. In addition, it has a strict requirement on operating conditions, since it is highly influenced by the polarization issue. Consequently, the development of a robust methodology for quantitative detection of Li plating in a commercial full cell under real-world operating coupled conditions presents a significant scientific and technical challenge.

In this contribution, we define a parameter $q_{Li(x,y)}$, termed the critical Li-plating areal capacity, derived from the impedance evolution characteristics in dynamic electrochemical impedance spectroscopy (DEIS) test under x ℃ and y C-rate charging conditions. Based on the $q_{Li(x,y)}$, an operando quantitative strategy for the

Li plating process in Graphite/$LiFePO_4$ (Gr/LFP) pouch cells is proposed. The efficacy, accuracy and universality of the strategy are further validated through the combined DEIS and operando solid-state NMR measurements, as well as the incremental capacity analysis across different temperatures (0, 25, 45 ℃), charging rates and battery configurations (4, 110 and 2300 mAh). The differences in Li plating characteristics and $q_{Li(x,y)}$ at various temperatures stem from the transition of Li nucleation-growth mechanism from progressive nucleation and three-dimensional growth (3DP) to instantaneous nucleation and two-dimensional growth (2DI) with increasing temperature. A transmission line model is further constructed to elucidate the physical essence of $q_{Li(x,y)}$. Finally, the battery aging processes under different coupled conditions with varying degree of Li plating severity are systematically studied, which reveals a strong correlation between $q_{Li(x,y)}$ and capacity plunge. Moreover, the Li plating boundary (LPB) advancing effect is identified as a critical factor that drive batteries from little Li plating to exceeding $q_{Li(x,y)}$ and experiencing capacity plunge during long-term cycling aging.

2. Results and discussion

Figure 1a illustrates the state-of-health (SOH) degradation of the Gr/LFP pouch cells (110 mAh nominal capacity) at a cycling protocol of 25 ℃, 3C charging and 1C discharging with different depth-of-charge (DOC). As the DOC increases from 27% to 44%, the SOH evolution changes from a non-degradation pattern to a non-linear aging pattern, i.e., capacity plunge. Evidently, a transition occurs in the dominant degradation mechanism, shifting from solid electrolyte interphase (SEI) growth to Li plating. Moreover, the higher the DOC, the earlier the emergence of the knee points in capacity degradation, and faster the capacity decay rates. The

accelerating effect on capacity degradation stems not only from the increased amount of plated Li, but also from a cascade of secondary issues triggered by the elevated Li plating levels. Therefore, it is of vital importance to quantitatively monitor the Li plating amount and evaluate the severity of Li plating.

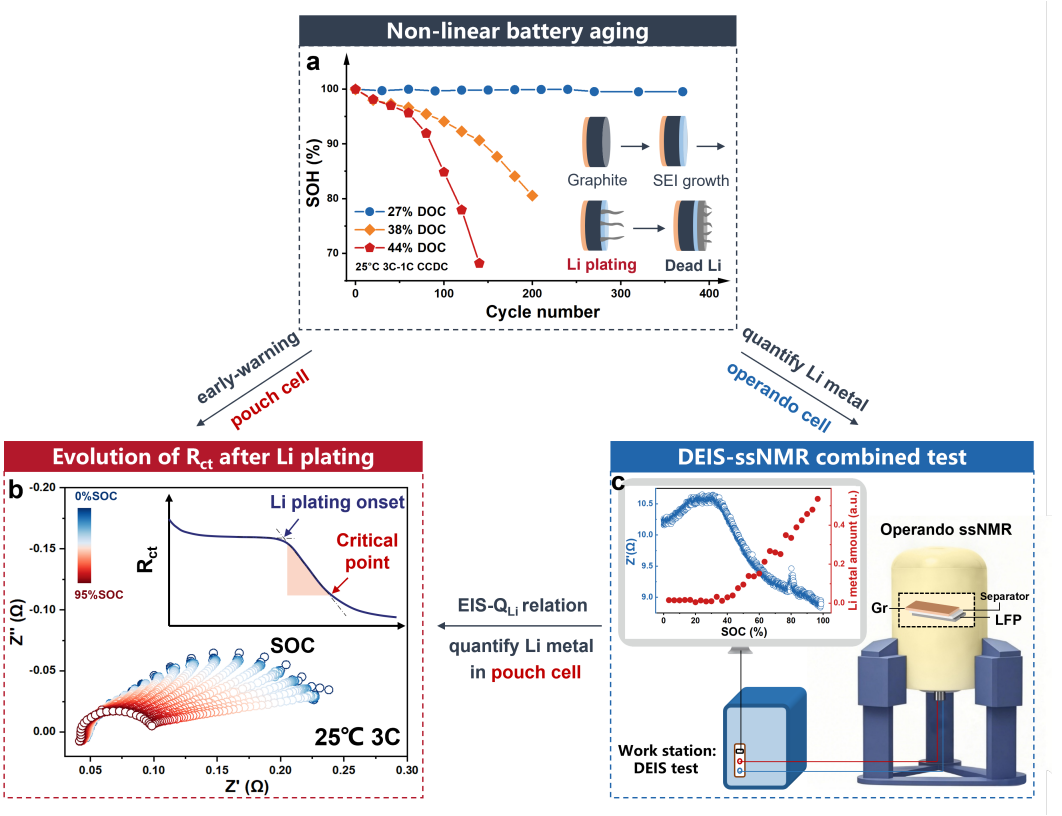


Figure 1. (a) Capacity degradation plots of Gr/LFP pouch cells under 25℃ 3C charging and 1C discharging with different DOC. (b) Evolution of Nyquist plots in the DEIS tests of Gr/LFP pouch cells under 25℃ 3C charging. The inset shows a schematic illustration of the R_{ct} variation trend during Li plating. (c) Schematic of the DEIS and ssNMR combined measurement for Li plating quantification. The inset shows the plots of Li plating amount growth (red, based on ssNMR) and real-part impedance variation at 5 Hz (blue, characteristic frequency of the charge transfer process) for the operando cell during charging at 25 ℃ and 2C.

DEIS has been demonstrated as an effective and sensitive technique for detecting the onset of Li plating in commercial LIB pouch cells. This is attributed to the features of a drastic contraction in Nyquist plots and a sudden drop in R_{ct} following the occurrence of Li plating (**Figure 1**b). **Figure S1** shows the great correspondence between this characteristic with Li plating by using the three-electrode cells to monitor the anode potential. **Figure S2** further verifies that this characteristic is reproducible across a broad range of temperatures (0, 25, and 45 ℃) and charge rates. However, quantitative detection of Li plating in pouch cells via impedance spectroscopy remains challenging, primarily owing to the ambiguous underlying physical mechanisms between impedance and Li metal capacity. In contrast, solid-state nuclear magnetic resonance (ssNMR) spectroscopy represents a more established operando technique for the quantitative analysis of Li plating [32-33]. By combining DEIS with operando ssNMR as shown in **Figure 3**, a comparison between the variation characteristics of impedance signals and the ssNMR-derived lithium metal content growth curves is obtained. The inset depicts the evolution of real-part impedance at 5 Hz (characteristic frequency of charge transfer process, reflecting R_{ct} [21]) and the Li plating capacity growth curve based on ssNMR spectra for the Gr/LFP operando cell during 2C charging at 25 ℃. Evidently, the onset of Li plating exhibits a high degree of overlap with the point of abrupt impedance decline. More notably, Li plating exhibits a linear growth trend, while the impedance response also features a linear segment at the initial stage of the abrupt decline. As illustrated in the schematic in the inset of **Figure 1**b, R_{ct} decreases rapidly in a linear manner first; after reaching a critical point, the downward trend of R_{ct} gradually decelerates. Therefore, it is imperative to conduct an in-depth investigation into the physical implications of the linear R_{ct} decline region associated with Li plating, and

to explore its potential for the quantitative characterization of Li plating.

To address the coupling issue between Li plating and intercalation processes under normal operating conditions, we design the experiment illustrated in **Figure 2**a. Three-electrode Gr/LFP pouch cells with excess cathode (N/P=0.67) were fabricated firstly. The graphite anode was then fully lithiated by controlling the graphite-to-reference electrode voltage to 0 V vs Li/Li^+ via a CC-CV procedure at 45 ℃ (to minimize polarization). After that, DEIS measurements were performed to overcharge the graphite, so that the correlation between R_{ct} evolution and overcharge capacity (i.e., Li plating capacity) is obtained. The evolution of the original Nyquist plots during the overcharging process is shown in **Figure S3**. The inset in **Figure 2**b presents the evolution of R_{ct} versus overcharge capacity at 25℃ and charging rates ranging from 1C to 3C. All these curves exhibit a characteristic pattern of an initial linear decline followed by a gradual stabilization, and they show good consistency across different charging rates. This observation indicates that the capacity corresponding to the linear region is relatively stable. Accordingly, we define a parameter $q_{Li(x,y)}$, termed the critical Li-plating areal capacity, which corresponds to the capacity within the interval from the starting point of the linear segment to the critical point where the linearity deviates, under charging conditions of x ℃ and y C-rate. Based on the principle, the $q_{Li(25,y)}$ values under different work conditions (from inset of **Figure 2**b) are summarized in **Figure 2**b. It gradually decreases with increasing charge rates, accounting for approximately 3% of the areal capacity of graphite anode (3 mAh cm^{-2}). It is worth noting that after normalization by areal capacity, the $q_{Li(x,y)}$ derived from the operando ssNMR model cell (~4mAh) tested at 25℃ and charging rates ranging from 1C to 2C (**Figure S5**) show good consistency with those from pouch cell (130mAh). This confirms the universality of

the established parameter, independent of battery configuration.

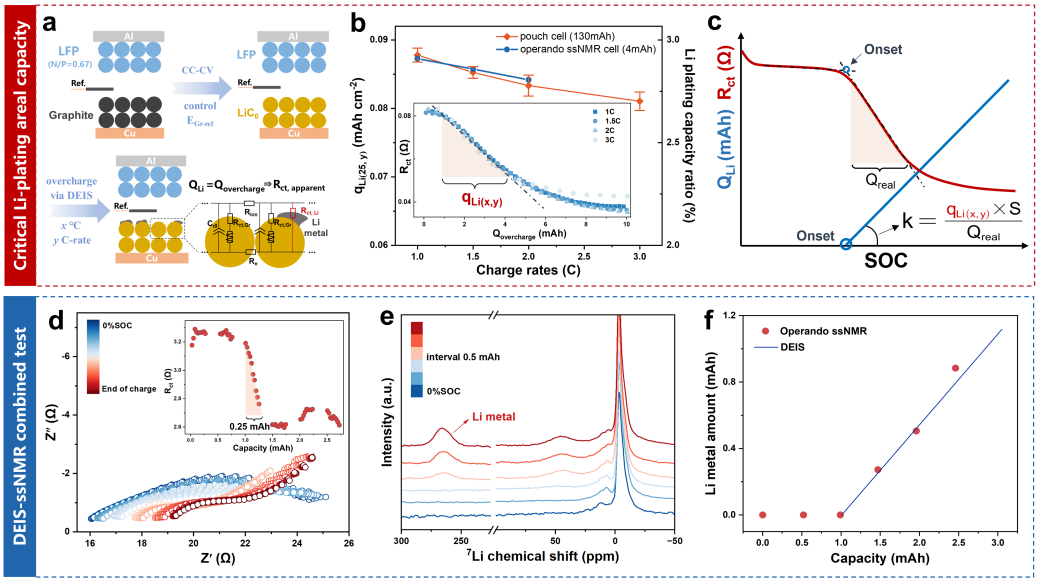


Figure 2. (a) Schematic of the quantitative determination of the critical Li-plating areal capacity, $q_{Li(x,y)}$, in three-electrode Gr/LFP cells (N/P=0.67), where x and y represent the charging temperature and rate, respectively. (b) Evolution of $q_{Li(25,y)}$ with charging rates, with the inset showing R_{ct} vs. $Q_{overcharge}$ profiles derived from DEIS tests at 25℃ and various charge rates. (c) Evolution of $q_{Li(x,y)}$ with charge rates at 25℃. Validation of the quantification strategy of Li plating by DEIS-ssNMR combined tests: Evolution of (d) Nyquist plots and as-fitted R_{ct} plots (inset), and (e) ssNMR spectra at 25℃ and 2C charging. (f) Comparison of the quantification results of Li plating based on ssNMR and DEIS.

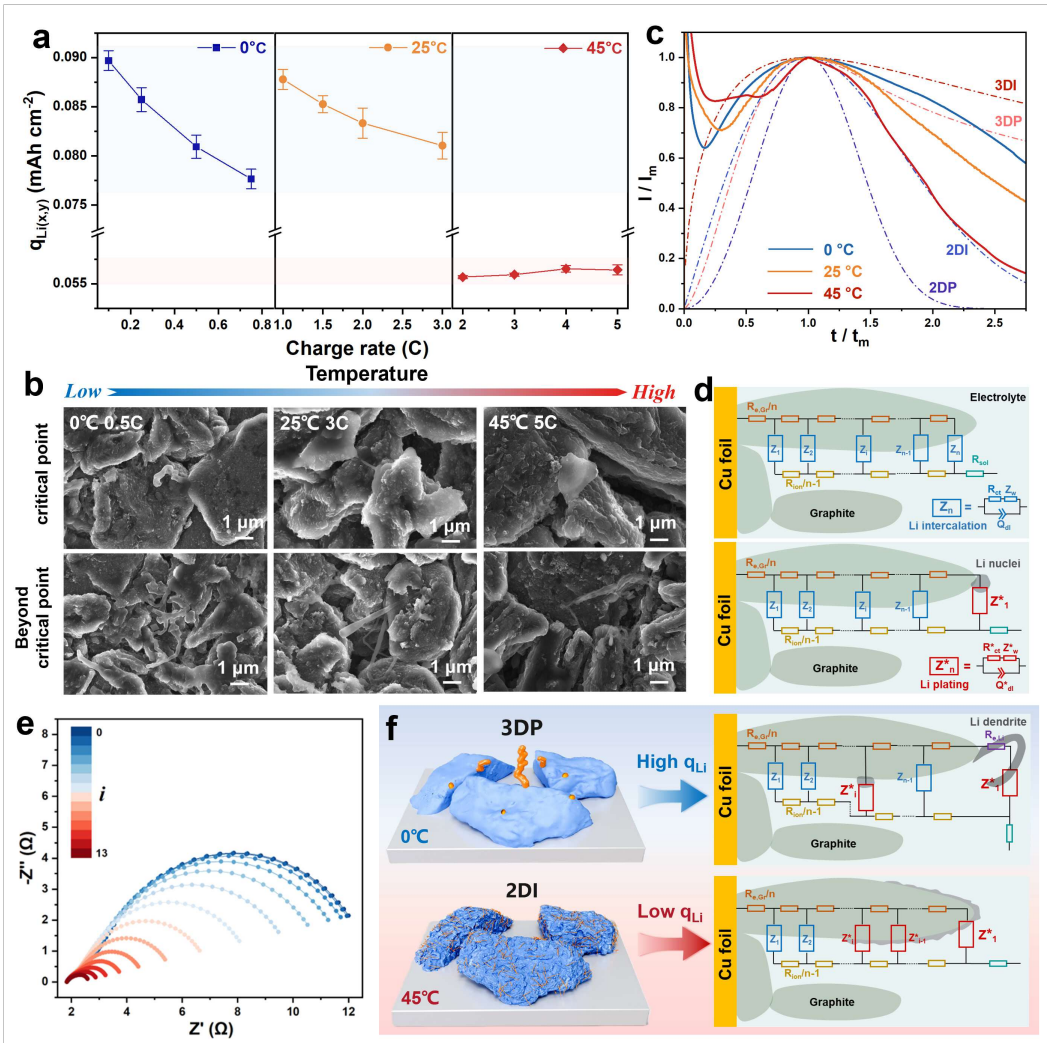
After defining and quantifying the parameter $q_{Li(x,y)}$, we further propose a Li plating quantification strategy for batteries with a normal N/P ratio, as schematized in **Figure 2**c. We first formulate a hypothesis that, for a given anode and charging protocol, the Li plating capacity must exceed $q_{Li(x,y)}$ to cause the R_{ct} decline to cross the critical point. As corroborated by the operando ssNMR data, the Li metal content

exhibits a linear growth trend subsequent to the occurrence of Li plating. Therefore, on the premise that the Li plating onset can be identified via the abrupt R_{ct} decline, the core challenge lies in determining the slope of the Li plating growth line. Based on the aforementioned hypothesis, the Li plating capacity (Q_{Li}) accumulated prior to the critical point can be obtained by multiplying $q_{Li(x,y)}$ by the anode area (S). The slope (k) of the Li plating growth curve could then be calculated as the ratio of Q_{Li} to the actual charging capacity (Q_{real}) within this interval.

To verify the feasibility and accuracy of this quantification strategy, we further conducted validation experiments using the combined DEIS and operando ssNMR characterization platform. The Gr/LFP operando ssNMR model cell with a normal N/P ratio of 1.09 was prepared firstly, and then charged at 25℃ and 2C with impedance and NMR spectra obtained simultaneously. The Nyquist plot of DEIS test in **Figure 2**d are fitted by a second-order Randles model, with the fitted R_{ct} evolution plot shown inset. It exhibits the same evolutionary trend as that observed in pouch cells: it firstly quickly decreases and then stabilizes. The gaps within the plot correspond to the acquisition time of ssNMR spectra. Based on the data in **Figure 2**b, the value of $q_{Li(25,2)}$ in operando cell equals to 0.0841 mAh·cm^{-2}. Thus, the Li plating rate is calculated as $q_{Li(25,2)}*S/Q_{total}$ = (0.0841 mAh·cm^{-2} ×1.62 cm^2) / 0.250 mAh= 0.545 mAh/mAh. **Figure 2**e exhibits the ssNMR spectra during the charging process, while the peaks located at 260 ppm that represents the signal of Li metal are used for Li plating quantification [32-33]. The calculated Li plating accumulation plots based on ssNMR and DEIS are compared in **Figure 2**f. The two plots exhibit high consistency with a calculated R^2 of 0.976. In another combined DEIS-ssNMR measurement case illustrated in **Figure S**6, despite discrepancies in both the onset and rate of Li plating between two operando cells, the Li plating

growth profiles derived from impedance and ssNMR still exhibit good consistency ($R^2 = 0.969$).

Since charging conditions exert a significant influence on the rate and characteristics of Li plating, we further investigated the variation law of $q_{Li(x,y)}$ under different temperatures and C-rates. The quantitative determination of $q_{Li(x,y)}$ at 0 ℃ with 0.1 to 0.75 C-rates and 45 ℃ with 2 to 5 C-rates was performed using the same method in **Figure 2**a, while the raw DEIS data and the fitted plots of R_{ct} evolution are presented in **Figure S3-4**. As shown in **Figure 3**a, the $q_{Li(x,y)}$ at 0 and 25 ℃ gradually decreases with increasing charge rates, and the variation ranges of the two are relatively close, both falling between 0.09 to 0.08 mAh cm^{-2}. In contrast, $q_{Li(x,y)}$ shows negligible variation with charge rates at 45 ℃, fluctuating around 0.055 mAh cm^{-2}, which is significantly lower than the values at 0 and 25 ℃. The features imply the Li plating behavior could be highly distinct between high temperatures and low temperatures. Furthermore, Gr/LFP pouch cells were charged to the critical point and beyond the critical point (exceeding 5.5 mAh, ~5% SOC) under three operating conditions (0 ℃ and 0.5C, 25 ℃ and 3C, 45 ℃ and 5C), followed by SEM characterization of the graphite surface morphology, as presented in **Figure 3**b. When charged to the critical point at 0 and 25 ℃, the graphite surface becomes significantly rougher compared to the pristine graphite (**Figure S7**), corresponding to the formation of Li nuclei, accompanied by the emergence of short Li dendrites. Further charging beyond the critical point drive the growth of them into dendrites with a high aspect ratio. In contrast, when charged to the critical point at 45 ℃, an uneven but uniformly coated Li layer formed on the graphite surface. Even with further charging beyond the critical point, the formed dendrites grow in a two-dimensional (2D) manner along the graphite surface.



253

254 **Figure 3.** (a) Evolution of $q_{Li(x,y)}$ with charging temperatures (0, 25, 45 ℃) and rates. (b) SEM
255 images of graphite anodes charged to the critical point (at $q_{Li(x,y)}$) and beyond critical point
256 (exceeding 5.5 mAh, ~5% SOC) at 0 ℃ 0.5C, 25 ℃ 3C and 45 ℃ 5C. (c) Dimensionless
257 current−time transients at different temperatures in comparison with the classical nucleation and
258 growth models. (d) Transmission line model (TLM) of the Li plating process on graphite anode
259 and (e) simulated evolution of Nyquist plots after Li plating. (f) Schematic of the influence of
260 temperatures on Li nucleation and growth mechanism and the value of $q_{Li(x,y)}$.

261

As the Li plating is basically an electrodeposition process, the nucleation and growth modes of Li metal on graphite could be analyzed through potentiostatic step experiments with the obtained *i~t* curves [34]. According to classical electrodeposition theory, nucleation and growth modes are categorized into progressive nucleation and instantaneous nucleation, three-dimensional growth) and two-dimensional growth, with corresponding equations (Equation 1~4) shown below.

$$3DI:\ \frac{I}{I_m}=\left(\frac{1.9542t_m}{t}\right)^{0.5}\left\{1-\exp\left[-1.2563\left(\frac{t_m}{t}\right)\right]\right\} \quad (1)$$

$$3DP:\ \frac{I}{I_m}=\left(\frac{1.2254t_m}{t}\right)^{0.5}\left\{1-\exp\left[-2.3367\left(\frac{t_m}{t}\right)^2\right]\right\} \quad (2)$$

$$2DI:\ \frac{I}{I_m}=\frac{t}{t_m}\exp\left\{\frac{1}{2}\left[1-\left(\frac{t}{t_m}\right)^2\right]\right\} \quad (3)$$

$$2DP:\ \frac{I}{I_m}=\left(\frac{t}{t_m}\right)^2\exp\left\{\frac{2}{3}\left[1-\left(\frac{t}{t_m}\right)^3\right]\right\} \quad (4)$$

Here, the I_m and t_m represent the peak current and time in the *i~t* curve. The standard *i~t* curves corresponding to distinct nucleation and growth mechanisms derived from four different equations are shown as the dashed lines in **Figure 3**c. To circumvent the interference from the coupled Li intercalation current, a strategy analogous to the method in **Figure 2**a was adopted, involving the full lithiation of the graphite anode followed by a constant voltage test. The processed data in **Figure 3**c reveals a transition from 3DP mode at 0 ℃ to 2DI mode at 45 ℃, with an intermediate mode observed at 25℃. This result also explains the phenomenon that localized dendrite growth readily occurs at 0/25 ℃, while Li nuclei are uniformly covered and undergo two-dimensional growth at 45 ℃. But how do the nucleation and growth modes and dendrites affect the impedance and $q_{Li(x,y)}$?

To unveil the physical meaning of impedance evolution during Li plating, a transmission line model (TLM) from a porous electrode perspective was constructed

to describe the Li plating process on graphite in **Figure 3**d [38-40]. The model initially comprises 100 pieces of $RC_{Li\ intercalation}$ elements, with the assumption that the formation of Li nuclei progressively displaces these units with $RC_{Li\ plating}$ elements and propagates across the graphite surface. Detailed description about the TLM is given in the Supporting Information. By increasing the numbers of the randomly replaced $RC_{Li\ plating}$ elements from 0 to 13, the impedance semicircle exhibits rapid but uniformly spaced shrinkage before gradually slowing down (**Figure 3**e), which precisely demonstrate the evolution characteristics that aligns with experimental observations. The TLM reveals that the decrease in R_{ct} indicates an increase in the coverage of Li nuclei on the graphite surface. Once it achieves a specific surface coverage threshold ($q_{Li(x,y)}$), the linear decreasing trend of R_{ct} is significantly decelerated. This finding can account for the substantial difference in $q_{Li(x,y)}$ between 0 ℃ and 45 ℃. As shown in **Figure 3**f, localized dendrite formation is more prone to occur at low temperatures, while the charge transfer process corresponding to dendrites is still governed by Li plating; this portion of capacity contributes minimally to the variation in R_{ct}. Consequently, a much higher capacity consumption is required to reach the aforementioned critical coverage value. At high temperatures, instantaneous nucleation enables a rapid coverage of graphite surface by Li nuclei, resulting in a smaller $q_{Li(x,y)}$. In addition, the effect of rate capability stems from the nucleation overpotential. **Figure S10** depicts the variation in lithium nucleation overpotential on the fully lithiated graphite surface with coupled operating conditions [41]. At 0 ℃, the nucleation overpotential increases from 14 mV to 35 mV as the rate rises from 0.1C to 0.75C. This induces the formation of more nucleation sites [42-43] and accelerates the coverage of lithium nuclei on the graphite surface, thus leading to a lower $q_{Li(x,y)}$. In contrast, at 45 ℃, the nucleation

overpotential only increases slightly from 9 mV to 10 mV when the rate increases from 2C to 5C. This negligible variation, combined with the instantaneous nucleation behavior to 45 ℃, results in a little change in $q_{Li(x,y)}$ with increasing rate at this temperature.

Although the accuracy of the Li-plating quantitative method has been validated via the DEIS-ssNMR combined experiment, ssNMR is not practically applicable to the high-capacity commercial pouch cells. Thus, the strategy illustrated in **Figure 4**d is adopted to further verify the effectiveness of this method for pouch cells under different coupled operating conditions. The destinations of the plated Li could be categorized into two parts: the reversible fraction undergoes electrochemical stripping during discharge, whereas the irreversible fraction converts to dead Li and residual-SEI. Accordingly, Equation 5 is given as follows.

$$Q_{\text{Li plating}} = Q_{\text{rev Li plating}} + Q_{\text{irrev Li plating}} = Q_{\text{Li strippping}} + \Delta Q_{\text{dead Li}} + \Delta Q_{\text{SEI}} \quad (5)$$

The irreversible part could be quantified by mass spectrometry titration (MST) [44-46], while the reversible part could be evaluated by the incremental capacity analysis (ICA).

Based on this strategy, we first performed validation experiments on 110 mAh Gr/LFP three-electrode pouch cells under three charging conditions: 0 ℃ and 0.5C, 25 ℃ and 3C, 45 ℃ and 5C. **Figure 4**a-c exhibit both the R_{ct} evolution during DEIS test and the accumulation of dead Li and residual-SEI derived from MST results under different DOC cutoff. For the 0 ℃ case (**Figure 4**a), no Li plating occurs at DOC below 30% SOC, and inactive Li showed almost no increase. After the onset of Li plating, a linear growth of dead Li is observed. Further charging, which caused the Li plating amount to exceed the threshold $q_{Li(x,y)}$, led to a sharp surge in both dead Li and residual-SEI contents. This indicates that there is a critical correlation

between the amount and reversibility of Li plating. When the Li plating amount exceeds $q_{Li(x,y)}$, dendrites form extensively (**Figure 3**b), resulting in considerable reversibility loss. The same trend was also observed in the quantitative MST results under 25 ℃/3C and 45 ℃/5C conditions.

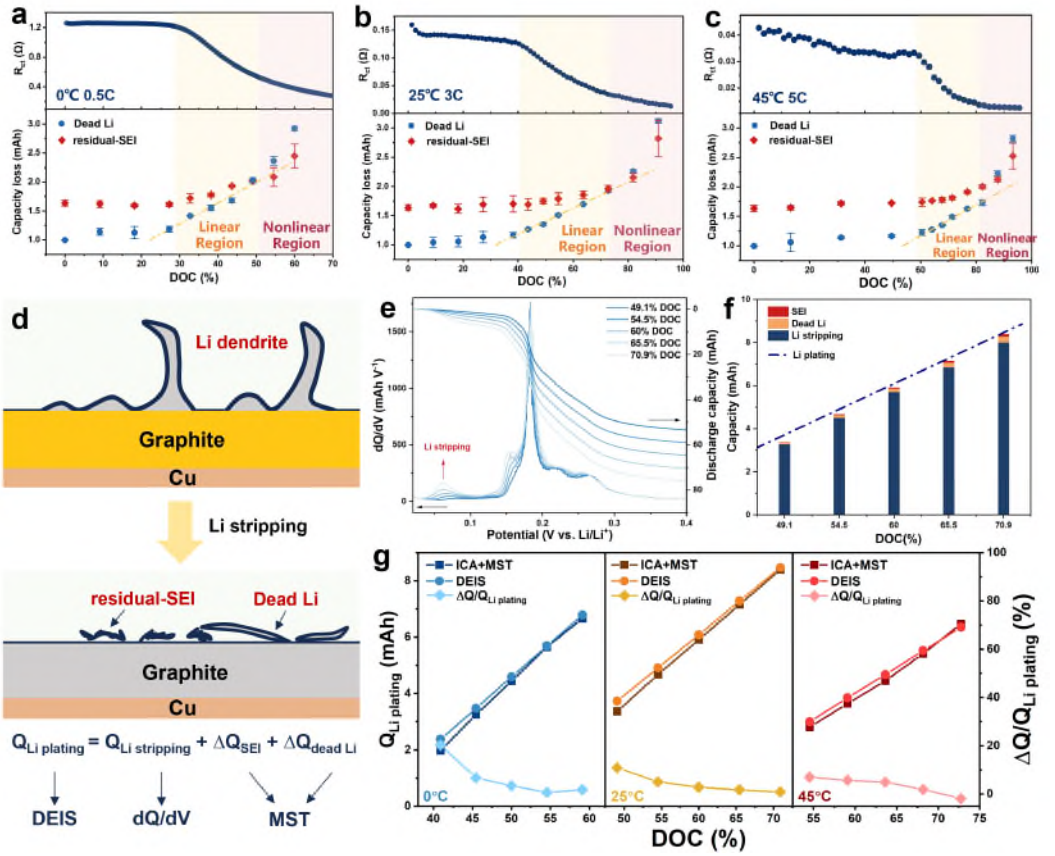


Figure 4. (a-c) Quantification results of dead Li and residual-SEI using MST in pouch cells cycled at (a) 0 ℃ and 0.5C, (b) 25 ℃ and 3C, (c) 45 ℃ and 5C with different DOC. (d) Schematic of the validation mechanism based on ICA and MST. (e) Discharge curves and dQ/dV curves of graphite anode at 25℃ and 3C charging with different DOC. (f) Comparison of quantifying results of Li plating based on DEIS and validating results based on ICA and MST. (g) Quantified Li plating curve, validated Li plating curve and relative error under three conditions (from left to right: 0 ℃ 0.5C, 25 ℃ 3C, 45 ℃ 5C) and different DOC.

After charging to specific SOC cut-offs with a different Li plating amount, the cells were discharged to obtain the voltage curves and dQ/dV curves of Gr anode. **Figure 4**e exhibits the dQ/dV curves of cells after charging at 25 ℃ and 3C. The peaks at around 0.06V, which correspond to the Li stripping process, have their integral taken as the capacity of reversible Li [29]. Based on Equation 1, the quantification results derived from DEIS and validation results calculated from ICA and MST are compared in **Figure 4**f. Obviously, the two results show great consistency with each other. Moreover, **Figure 4**g concludes the comparison between Li plating quantitative results with validated results, as well as the relative error, at different temperatures. The two plots show good consistency with relative errors below 10% in most cases. Furthermore, the quantitative validation tests of Li plating on a 2300mAh Gr/LFP pouch cell at different temperatures also show general consistency except for the 45 ℃ (**Figure S12-13**). The discrepancy between the quantified and validation results may arise from two factors: First, quantifying the capacity of reversible plated Li from discharge curves can be affected by polarization effects (discharge rates) and chemical re-intercalation of plated Li, as detailed in the Supporting information and **Figure S14**. Second, the deeper discharge state achieved with CC-CV protocol before MST tests might lead to a little underestimation of the actual capacity of irreversible plated Li. In short, the two validation strategies from prove the generality and accessibility of this quantification strategy across varied work conditions and battery configurations.

To systematically evaluate Li plating's impact on battery life, we conducted cycling tests under varied temperatures, charge rates, and Li plating degrees. Capacity cutoff conditions were strategically selected based on the R_{ct} evolution in

DEIS tests to achieve four different severity of Li plating: no plating, little (exceed Li plating onset), middle (midpoint of linear region), and severe (exceed $q_{Li(x,y)}$), as detailed in **Table S2**. The Li plating amount is comparable under the same setup with the same Li plating degree at different temperatures. All cells were cycled to below 80% SOH, and reference performance tests (RPT) were performed at regular cycle intervals. The RPT protocol includes DEIS measurements to track the evolution of the Li plating boundary (LPB) throughout cycling, as well as fast galvanostatic intermittent titration technique (GITT) measurements for thermodynamic diagnostics with Li inventory loss (LLI) and active material loss (LAM) quantified [46-47].

Figure 5a depict the evolution of SOH under the condition of 0°C and 0.5C charging and 0.5C discharging, with four cutoff conditions (18%, 32%, 36%, 54% DOC, corresponding to different Li plating degrees). The thermodynamic diagnosis results in **Figure S16** demonstrate that LLI dominate the capacity degradation at all cycling protocols, suggesting that Li plating is the dominant degradation mechanism. At the cutoff conditions of 32% and 36% DOC, the capacity degradation exhibits a staged characteristic: an initial linear degradation phase followed by a nonlinear capacity plunge. When the cutoff condition at 54% DOC results in the Li plating amount exceeding the threshold $q_{Li(x,y)}$, the battery undergoes rapid capacity degradation from the very onset of cycling, which persists until the battery reaches its end-of-life. **Figure 5**b further illustrates the detailed LPB evolution during battery aging with a 36% DOC cutoff. The onset of LPB advances progressively, causing the Li plating amount to exceed $q_{Li(x,y)}$ during the 8th and 9th RPT diagnosis, which exactly coincides with the knee point observed in **Figure 5**a. The result indicates a strong correlation between Li plating amount exceeding the critical threshold $q_{Li(x,y)}$

and the capacity plunge during Li plating-dominated battery aging. To comprehensively illustrate the interrelationships among Li plating boundary (LPB) and battery aging, the data across all operating conditions are presented in **Figure S15-16**, and summarized in **Figure 5**c. **Figure 5**c presents two paired bars for each cycling protocol. The left bar illustrates the evolution of SOH, while the right bar depicts the progression of the LPB. The reduction of left color block corresponds to accelerated SOH degradation, while the reduction of right color represents an accelerated advancing rate of LPB. Comparative analysis reveals that the batteries always experience capacity plunge whenever the LPB is advanced to result in the Li plating amount exceeding the critical value $q_{Li(x,y)}$, regardless of the temperature and initial Li plating severity.

The effect of Li plating on battery aging can be summarized in **Figure 5**d. When Li plating occurs, the battery deviates from the original linear degradation regime governed by SEI growth and exhibits a quasi-linear accelerated degradation. At this stage, despite a low Li plating amount, LPB advances continuously with aging until the Li plating amount exceeds $q_{Li(x,y)}$, triggering the capacity plunge. The LPB advancing effect during battery aging stems from two factors as illustrated in **Figure 5**e. First, dead Li on the graphite surface reduces the lithium nucleation overpotential and accelerates the nucleation process. In **Figure S18**, the nucleation overpotential of the Li/Gr three-electrode half-cell at the 2nd cycle is reduced by 78%, 47% and 33% compared with the 1st cycle at 0, 25 and 45 °C under a current density of 1 mA cm^{-2}. In addition, dead Li hinders Li^+ transport and increases polarization. Thus, the re-evaluation of LPB and adjustment of cycling protocol is critical for prolong battery remaining useful life.

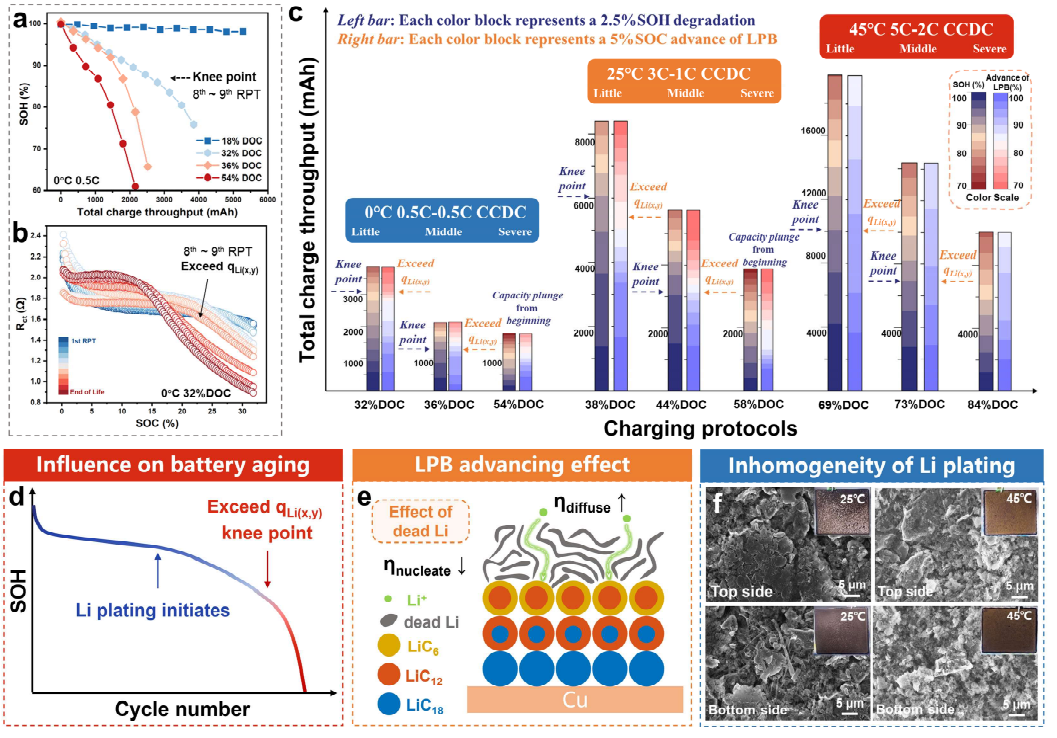


Figure 5. Capacity degradation of Gr/LFP pouch cell at 0°C 0.5C charging with different DOC. (b) R_{ct} change derived from the DEIS tests in the RPT during aging at 0°C 0.5C charging with 32% DOC. (c) Electrochemical performance of Gr/LFP batteries at different cycling protocols. Left bar: SOH degradation. Right bar: LPB evolution. (d) Relation between Li plating and $q_{Li(x,y)}$ with non-linear aging characteristics of LIBs. (e) Mechanistic scheme of LPB advancing effect. (f) Inhomogeneity feature of Li plating: optical and SEM images of the top side and bottom side of the graphite electrode aged under 25 °C and 45°C.

It should be noted that, benefiting from the 2DI nucleation and growth mechanism at 45 °C, the accelerated capacity decay induced by Li plating at elevated temperatures is significantly mitigated compared with that at room and low temperatures. The optical and SEM images of the double-sided graphite anodes after the cells aged to the end-of-life are shown in **Figure S19-21**, which reveal a distinct

difference between the 45℃ condition and the 0/25 ℃ conditions. As shown in **Figure 5**d, Li plating on graphite displays a pronounced inhomogeneity under the 0/25 ℃. The anode's top surface has large silvery metal patches, proven to be the agglomerates of Li blocks sized from tens to hundreds of micrometers by SEM. There's no visible metal on the bottom surface. The SEM images show the presence of a large number of Li dendrites but no Li blocks. This phenomenon is consistently observed across all cells aged at 0/25 ℃, whereas no such feature was detected in those aged at 45 ℃. Both electrode sides exhibit fragmented dead Li, with the absence of large-scale Li agglomerates. At 0/25 ℃, when the Li plating capacity exceeds $q_{Li(x,y)}$, the massive Li dendrites with 3D-growth characteristics induce severe side reactions, triggering gas generation, electrolyte and additive decomposition [48-49]. These side reactions cause local electrolyte drying-up and increase the local current density, which exacerbates localized Li plating and thus gives rise to a positive feedback loop, ultimately leading to the formation of large Li agglomerates and rapid cell failure. We hypothesize that the morphological discrepancy of Li metal between the upper and lower surfaces arises from the effect of gravity, whereby the microbubbles generated inside the cell are more stable on the upper surface, while those on the lower surface diffuse away and are replenished by the electrolyte. These observations indicate that capacity degradation is associated not merely with the amount of plated Li, but its morphology also serves as a pivotal triggering factor.

3. Conclusion

This study proposes an operando quantitative methodology to elucidate Li plating dynamics on graphite anodes, demonstrating broad applicability across

diverse coupled operational conditions. Central to this approach is the definition of a critical parameter, $q_{Li(x,y)}$ (defined as the critical Li-plating areal capacity derived from dynamic electrochemical impedance spectroscopy (DEIS) measurements), enabling precise calculation of linear Li plating rates and facilitating extrapolation of cumulative Li deposition curves from the onset of plating events. Comprehensive validation through operando solid-state nuclear magnetic resonance (ssNMR) coupled with DEIS measurements, alongside independent corroboration via incremental capacity analysis (ICA) and mass spectrometry titration (MST), confirms the method's robustness with excellent efficacy ($R^2 > 0.97$) and remarkable accuracy (<10% deviation) across extended temperature ranges (0–45°C) and multiple battery architectures (4 mAh operando cells, 110 mAh pouch cells, and 2.3 Ah commercial-scale cells). Transmission line model (TLM) analysis reveals that $q_{Li(x,y)}$ corresponds to the minimum capacity required for complete surface coverage of graphite by Li nuclei. Remarkably, elevated temperatures (> 45°C) induce a mechanistic transition from three-dimensional (3DP) to two-dimensional (2DI) nucleation-growth patterns, substantially reducing $q_{Li(x,y)}$ values by ~40% through enhanced nucleation rates. Accelerated aging experiments systematically investigate Li plating-induced degradation under coupled operational stresses. A pivotal observation is the progressive advancement of the Li plating boundary (LPB), where initial mild plating accelerates capacity fade through electrodeposition-induced mechanical stress, ultimately propelling LPB migration beyond the critical threshold ($q_{Li(x,y)}$) and triggering catastrophic capacity loss (>30% within 50 cycles). It highlights the necessity of monitoring Li plating status and boundary variation during the batteries' service period to prolong battery life and ensure battery safety.

Acknowledgements

W.H. and J.L. contributed equally to this work. This work was supported by the National Key R&D Program of China (grant no. 2021YFB2401800).

Conflict of Interest

The authors declare no competing financial interest.

Data availability

Data for this article are available at Zenedo at doi.org/10.5281/zenodo.19350624.

Reference

1. Xiao, J. How lithium dendrites form in liquid batteries. *Science* **366** 426-427 (2019). https://doi.org/10.1126/science.aay8672
2. Tarascon, JM., Armand, M. Issues and challenges facing rechargeable lithium batteries. *Nature* **414**, 359–367 (2001). https://doi.org/10.1038/35104644
3. Palacín, M. R.,Guibert, A. D. Why do batteries fail? *Science* **351**, 1253292 (2016). https://doi.org/10.1126/science.1253292
4. Konz, Z.M., Wirtz, B.M., Verma, A. et al. High-throughput Li plating quantification for fast-charging battery design. *Nat. Energy* **8**, 450–461 (2023). https://doi.org/10.1038/s41560-023-01194-y
5. Liu, Y., Zhu, Y. & Cui, Y. Challenges and opportunities towards fast-charging battery materials. *Nat. Energy* **4**, 540–550 (2019). https://doi.org/10.1038/s41560-019-0405-3
6. Hu, X., Xu, L., Lin, X., Pecht, M. Battery lifetime prognostics. *Joule* **19**, 310-346 (2020). https://doi.org/10.1016/j.joule.2019.11.018

7. Lin, X., Khosravinia, K., Hu, X. et al. Lithium Plating Mechanism, Detection, and Mitigation in Lithium-Ion Batteries. *Prog. Energy Combust. Sci.* **87**, 100953 (2021). https://doi.org/10.1016/j.pecs.2021.100953
8. Yang, Y., Xu, L., Yan, C. Huang, J., Zhang, Q. Towards the intercalation and lithium plating mechanism for high safety and fast-charging lithium-ion batteries: a review. *Energy Lab* **1**, 220011 (2023). https://doi.org/10.54227/elab.20220011
9. Mijailovic, A. S., Waag-Swift, S., Wang, G. et al. Interplay of intercalation dynamics and lithium plating in monolithic and architectured graphite anodes during fast charging. *Energy Environ. Sci.* **17**, 8702-8721 (2024). https://doi.org/10.1039/D4EE02211D
10. Gao, T, Han, Y., Fraggedakis, D. et al. Interplay of Lithium intercalation and plating on a single graphite particle. *Joule* **5**, 393-414 (2021). https://doi.org/10.1016/j.joule.2020.12.020
11. Cooper, E. R., Li, M., Gentle, I. et al. A Deeper Understanding of Metal Nucleation and Growth in Rechargeable Metal Batteries Through Theory and Experiment. *Angew. Chem. Int. Ed.* **62**, e202309247 (2023). https://doi.org/10.1002/anie.202309247
12. Rangarajan, S. P., Barsukov, Y., Mukherjee, P. P. Plating energy as a universal descriptor to classify accelerated cell failure under operational extremes. *Cell Rep. Phys, Sci.* **3** 100720 (2022). https://doi.org/10.1016/j.xcrp.2021.100720
13. Raj, A., Rodrigures, M. T., Abraham, D. P. Rate-dependent ageing resulting from fast charging of Li-ion cells. *J. Electrochem. Soc.* **167**, 12057 (2020). https://doi.org/10.1149/1945-7111/abace9
14. Weng, S., Yang, G., Zhang, S. et al. Kinetic limits of graphite anode for fast-charging Lithium-ion batteries. *Nano-Micro Lett.* **15** 215 (2023).

https://doi.org/10.1007/s40820-023-01183-6

15. Paul, P. P., McShane, E. J, Colclasure, A. M. et al. A Review of Existing and Emerging Methods for Lithium Detection and Characterization in Li-Ion and Li-Metal Batteries. *Adv Energy Mater.* **11**, 2100372 (2021) https://doi.org/10.1002/aenm.202100372
16. Tian, Y., Lin, C., Li, H. et al. Detecting undesired lithium plating on anodes for lithium-ion batteries-A review on the in-situ methods. *Applied Energy* **300**, 117386(2021). https://doi.org/10.1016/j.apenergy.2021.117386
17. Waldmann, T., Hogrefe, C., Flugel M. et al. Efficient Workflows for Detecting Li Depositions in Lithium-Ion Batteries. *J. Electrochem. Soc.* **171**, 070526 (2024). https://doi.org/10.1149/1945-7111/ad5ef8
18. Brown, D., McShane, E., Konz, Z., et al. Detecting Onset of Lithium Plating During Fast Charging of Li-ion Batteries Using *Operando* Electrochemical Impedance Spectroscopy. *Cell Rep. Phy. Sci.* **10**, 100589 (2021). https://doi.org/10.1016/j.xcrp.2021.100589
19. Chen, X., Li, L., Liu, M., et al. Detection of Lithium Plating in Lithium-ion Batteries by Distribution Relaxation Times. *J. Power Sources* **496**, 229857 (2021). https://doi.org/10.1016/j.jpowsour.2021.229867
20. Lin, Y, Hu, W., Ding, M., et al. Unveiling the Three Stages of Li Plating and Dynamic Evolution Processes in Pouch C/$LiFePO_4$ Batteries. *Adv Energy Mater.* **14**, 2400894 (2024) https://doi.org/10.1002/aenm.202400894
21. Xu, L., Xiao, Y., Yang, Y. et al. Operando quantified Lithium plating determination enabled by dynamic capacitance measurement in working Li-ion batteries. *Angew. Chem. Int. Ed.* **61**, e202210365 (2022). https://doi.org/10.1002/anie.202210365

22. Xu, L., Yan, C., Huang, J. Q., et al. In-Situ Li plating diagnosis for fast-charging Li-ion batteries enabled by relaxation time detection. *Adv. Mater.* **35**, 2301881 (2023). https://doi.org/10.1002/adma.202301881

23. Hu, W., Peng, Y., Wei, Y., Yang, Y. Application of electrochemical impedance spectroscopy to degradation and ageing research of Lithium-ion batteries. *J. Phys. Chem. C* **127**, 4465-4495 (2023). https://doi.org/10.1021/acs.jpcc.3c00033.

24. Huang, W., Ye, Y., Chen, H. et al. Onboard early detection and mitigation of lithium plating in fast-charging batteries. *Nat. Commun*. **13**, 7091 (2022). https://doi.org/10.1038/s41467-022-33486-4

25. Bitzer, B., Gruhle, A. A new method for detecting lithium plating by measuring the cell thickness. *J. Power Sources* **262**, 297-302 (2014). https://doi.org/10.1016/j.jpowsour.2014.03.142

26. Konz, Z. M., McShane, E. J, McCloskey, B. D. Detecting the Onset of Lithium Plating and Monitoring Fast Charging Performance with Voltage Relaxation. *ACS Energy Lett.* **5**, 1750-1757 (2020). https://dx.doi.org/10.1021/acsenergylett.0c00831

27. Petzl, M., Danzer, M. A. Nondestructive detection, characterization, and quantification of lithium plating in commercial lithium-ion batteries. *J. Power Sources* **254** 80-87 (2014). https://doi.org/10.1016/j.jpowsour.2013.12.060

28. Burns, J. C., Stevens, D. A., Dahn, J. R. In-Situ Detection of Lithium Plating Using High Precision Coulometry. *J. Electrochem Soc.* **162**, 959-964 (2015). https://doi.org/10.1149/2.0621506jes

29. Mei, W., Jiang, L., Liang, C. et al. Understanding of Li-plating on graphite electrode: detection, quantification and mechanism revelation. *Energy Storage Mater.* **41**, 209-221 (2021) https://doi.org/10.1016/j.ensm.2021.06.013

30. Wasylowski, D., Ditler, H., Sonnet, M. et al. Operando visualisation of lithium plating by ultrasound imageing of battery cells. *Nat. Commun*. **15**, 10237 (2024). https://doi.org/10.1038/s41467-024-54319-6.
31. Huang, Y., Perlmutter, D., Fei-Huei Su, A. et al. Detecting lithium plating dynamics in a solid-state battery with *operando* X-ray computed tomography using machine learning. *npj Comput Mater* **9**, 93 (2023). https://doi.org/10.1038/s41524-023-01039-y
32. Zhou, Y., Lin, H., Zhong, C., et al. Long-Term Operando Quantification of Li Plating on Graphite Anodes. *J. Am. Chem. Soc.* **147**, 43529–43539 (2025). https://doi.org/10.1021/jacs.5c12037
33. Lin, H., Hu, Y., Zhou, Y., et al. Unveiling the Onset, Evolution, and Kinetic Factors Associated with Lithium Plating on Graphite Electrodes in Lithium-ion Batteries. *Adv. Energy Mater.* **15**, e02728 (2025) https://doi.org/10.1002/aenm.202502728
34. Thirumalraj, B., Hagos, T. T., Huang, C. J. et al. Nucleation and growth mechanism of Lithium metal electroplating. *J. Am. Soc. Chem.* **141**, 18612-18623 (2019). https://doi.org/10.1021/jacs.9b10195
35. Yao, Y. X., Wan, J., Liang, N. Y, Yan, C., Wen, R., Zhang, Q. Nucleation and growth mode of solid electrolyte interphase in Li-ion batteries *J. Am. Chem. Soc.* **145** 8001-8006 (2023). https://doi.org/10.1021/jacs.2c13878
36. Milchev, A., Krastev, I. Two-dimensional progressive and instantaneous nucleation with overlap: The case of multi-step electrochemical reactions. *Electrochim. Acta* **56** 2399-2403 (2011). http://dx.doi.org/10.1016/j.electacta.2010.11.025
37. Scharifker, B. R., Hills, G. Theoretical and experimental studies of multiple

nucleation. *Electrochim. Acta* **28** 879-889 (1983). https://doi.org/10.1016/0013-4686(83)85163-9

38. Talian, S. D., Bobnar, J., Sinigoj, A. R., Humar, I., Gaberšček, M. Transmission line model for description of the impedance response of Li electrodes with dendritic growth. *J. Phys. Chem. C* **123**, 27997-28007 (2019). https://doi.org/10.1021/acs.jpcc.9b05887
39. Ogihara, N., Itou, Y., Tsuyoshi, S., Takeuchi, Y. Impedance Spectroscopy Characterization of Porous Electrodes under Different Electrode Thickness Using a Symmetric Cell for High-Performance Lithium-Ion Batteries. *J. Phys. Chem. C* **119**, 4612-4619 (2015). https://pubs.acs.org/doi/10.1021/jp512564f
40. Gaberšček, M. Impedance spectroscopy of battery cells: Theory versus experiment. *Curr. Opin. Electrochem.* **32**, 100917 (2022). https://doi.org/10.1016/j.coelec.2021.100917
41. Mohammadi, A., Monconduit, L., Stievano, L., Younesi, R. Measuring the Nucleation Overpotential in Lithium Metal Batteries: Never Forget the Counter Electrode! *J. Electrochem. Soc.* **169**, 070509 (2022). https://doi.org/10.1149/1945-7111/ac7e73
42. Liu, X., Wang, G., Lv, Z., et al. A Perspective on Uniform Plating Behavior of Mg Metal Anode: Diffusion Limited Theory versus Nucleation Theory. *Adv. Mater.* **36** 2306395 (2024) https://doi.org/10.1002/adma.202306395
43. Pei, A., Zheng, G., Shi, F., et al. Nanoscale Nucleation and Growth of Electrodeposited Lithium Metal. *Nano Lett.* **17** 1132-1139 (2017). http://dx.doi.org/10.1021/acs.nanolett.6b04755
44. Tao, M., Xiang, Y., Zhao, D. *et al.* Protocol for quantifying inactive lithium in anode-free lithium batteries by mass spectrometry titration. *Commun Mater* **3**,

50 (2022). https://doi.org/10.1038/s43246-022-00273-z

45. Fang, C., Li, J., Zhang, M. *et al.* Quantifying inactive lithium in lithium metal batteries. *Nature* **572**, 511–515 (2019). https://doi.org/10.1038/s41586-019-1481-z

46. Peng, Y., Zhong, C., Ding, M. et al. Quantitative Analysis of Active Lithium Loss and Degradation Mechanism in Temperature Accelerated Ageing Process of Lithium-Ion Batteries. *Adv. Funct. Mater.* **34**, 2404495 (2024). https://doi.org/10.1002/adfm.202404495

47. Peng, Y., Ding, M., Zhang, K. et al. Quantitative analysis of the coupled mechanisms of lithium plating, SEI growth, and electrolyte decomposition in fast charging battery. *ACS Energy Lett.* **9**, 6022-6028 (2024). https://doi.org/10.1021/acsenergylett.4c02898

48. Liao, Y., Zhang, H., Peng, Y., et al. Electrolyte Degradation During Aging Process of Lithium-Ion Batteries: Mechanisms, Characterization, and Quantitative Analysis. *Adv. Energy Mater.* **14**, 2304295 (2024). https://doi.org/10.1002/aenm.202304295

49. Zhang, H., Peng, Y., Hu, Y., et al. Quantitative Analysis of Aging and Rollover Failure Mechanisms of Lithium-Ion Batteries at Accelerated Aging Conditions. *Adv. Energy Mater.* **15**, 2404997 (2025). https://doi.org/10.1002/aenm.202404997.

Supplementary Files

This is a list of supplementary files associated with this preprint. Click to download.

- Supportinginformation1.docx